


# Enhancement of Electrical Conduction and Phonon Scattering in $\text{Ga}_2\text{O}_3(\text{ZnO})_9$ - $\text{In}_2\text{O}_3(\text{ZnO})_9$ Compounds by Modification of Interfaces at the Nanoscale

DIANA T. ALVAREZ-RUIZ,<sup>1</sup> FERIDOON AZOUGH,<sup>1</sup>  
DAVID HERNANDEZ-MALDONADO,<sup>2</sup> DEMIE M. KEPAPTSOGLU,<sup>2</sup>  
QUENTIN M. RAMASSE,<sup>2</sup> PETER SVEC,<sup>3</sup> PETER SVEC SR.,<sup>3</sup>  
and ROBERT FREER <sup>1,4</sup>

1.—School of Materials, University of Manchester, Manchester M13 9PL, UK. 2.—SuperSTEM Laboratory, STFC Daresbury Campus, Daresbury WA4 4AD, UK. 3.—Institute of Physics, Slovak Academy of Sciences, 845 11 Bratislava, Slovak Republic. 4.—e-mail: Robert.Freer@manchester.ac.uk

The  $\text{Ga}_2\text{O}_3(\text{ZnO})_9$  and  $\text{In}_2\text{O}_3(\text{ZnO})_9$  homologous phases have attracted attention as thermoelectric (TE) oxides due to their layered structures.  $\text{Ga}_2\text{O}_3(\text{ZnO})_9$  exhibits low thermal conductivity, while  $\text{In}_2\text{O}_3(\text{ZnO})_9$  possesses higher electrical conductivity. The TE properties of the solid solution of  $\text{Ga}_2\text{O}_3(\text{ZnO})_9$ - $\text{In}_2\text{O}_3(\text{ZnO})_9$  were explored and correlated with changes in the crystal structure. High-quality  $(1-x)\text{Ga}_2\text{O}_3(\text{ZnO})_9$ - $(\text{ZnO})_9$  ( $x = 0.0$  to  $1.0$ ) ceramics were prepared by the solid-state route using  $\text{B}_2\text{O}_3$  and  $\text{Nd}_2\text{O}_3$  as additives. The crystal structures were analysed by x-ray diffraction, high-resolution transmission electron microscopy and atomic resolution scanning transmission electron microscopy—high-angle annular dark field imaging—energy dispersive x-ray spectroscopy (STEM-HAADF-EDS) techniques. A layered superstructure with compositional modulations was observed in all samples in the  $(1-x)\text{Ga}_2\text{O}_3(\text{ZnO})_9$ - $x\text{In}_2\text{O}_3(\text{ZnO})_9$  system. All the ceramics exhibited nanoscale structural features identified as Ga- and In-rich inversion boundaries (IBs). Substitution of 20 mol.% In ( $x = 0.2$ ) in the  $\text{Ga}_2\text{O}_3(\text{ZnO})_9$  compounds generated basal and pyramidal indium IBs typically found in the  $\text{In}_2\text{O}_3(\text{ZnO})_m$  system. The  $(\text{Ga}_{0.8}\text{In}_{0.2})_2\text{O}_3(\text{ZnO})_9$  compound does not exhibit the structural features of the *Cmcm*  $\text{Ga}_2\text{O}_3(\text{ZnO})_9$  compound, which is formed by a stacking of Ga-rich IBs along the pyramidal plane of the wurtzite ZnO, but features that resemble the crystal structure exhibited by the *R $\bar{3}m$*   $\text{In}_2\text{O}_3(\text{ZnO})_m$  with basal and pyramidal indium IBs. The structural changes led to improved TE performance. For example,  $(\text{Ga}_{0.8}\text{In}_{0.2})_2\text{O}_3(\text{ZnO})_9$  showed a low thermal conductivity of 2 W/m K and a high power factor of  $150 \mu\text{W}/\text{m K}^2$  giving a figure of merit (*ZT*) of 0.07 at 900 K. This is the highest *ZT* for  $\text{Ga}_2\text{O}_3(\text{ZnO})_9$ -based homologous compounds and is comparable with the highest *ZT* reported for  $\text{In}_2\text{O}_3(\text{ZnO})_9$  homologous compounds.

**Key words:** ZnO, thermoelectric, homologous compounds, interfaces, inversion boundaries, twin boundaries

## INTRODUCTION

To minimise the environmental impact of power generation from fossil fuels, alternative sources are being investigated. Thermoelectrics (TEs) have

received much attention because they can be used to generate electrical power from waste heat without releasing  $\text{CO}_2$ . For many years, Pb- and Te-based alloys have been extensively investigated<sup>1</sup> for TE applications as they exhibit low thermal conductivity ( $\kappa$ ) and relatively high electrical conductivity ( $\sigma$ ) and Seebeck coefficients ( $S$ ), which are necessary for good TE performance. Candidate materials are usually evaluated in terms of the dimensionless figure of merit  $ZT$ <sup>2,3</sup> given by  $ZT = S^2 \sigma / \kappa$ . To maximise the energy generated by TEs, both  $n$ - and  $p$ -type elements are connected electrically in series and thermally in parallel within a TE module. The inherent toxicity, high cost and poor (high temperature) thermal stability of Te- and Pb-based alloys have limited the large-scale application of TE modules based on such materials. As alternatives to these well-known TE materials, oxides are attractive candidates because of their stability in air at high temperatures and low toxicity. However, their low electrical conductivity and high thermal conductivity limits their TE efficiency. Many attempts have been made to lower the thermal conductivity of well-known TE oxides through nanostructuring.<sup>4</sup>

The naturally occurring superlattice structures found in the  $\text{ZnO-In}_2\text{O}_3$  and  $\text{ZnO-Ga}_2\text{O}_3$  systems has prompted interest in them as  $n$ -type oxide TEs.<sup>5-7</sup> The  $\text{Ga}_2\text{O}_3(\text{ZnO})_m$ ,  $\text{In}_2\text{O}_3(\text{ZnO})_m$  and  $\text{InGaO}_3(\text{ZnO})_m$  ( $m = \text{integer}$ ) modular compounds are characterised by a stacked series of interfaces such as twin and inversion boundaries (IBs) along their  $c$  axis,<sup>6,8</sup> which lowers the thermal conductivity, with respect to that of  $\text{ZnO}$ , by an order of magnitude.<sup>5,6,8</sup> The layered structures of these compounds enable good electrical conductivity in one direction, whilst maintaining effective scattering of phonons at the interfaces. This leads to enhanced  $ZT$  values when the anisotropy of these compounds is exploited by texturing.<sup>9</sup> A further advantage of these superlattice structures is the ease with which the width of the interfaces (structural modules) can be modified by changing the value of  $m$ , and thereby tuning their TE properties.

There have been limited studies of the TE properties and crystal structures of  $\text{Ga}_2\text{O}_3(\text{ZnO})_m$ . In an early high-resolution transmission electron microscopy (HRTEM) study, Li et al.<sup>10</sup> proposed a crystal structure for the end members with  $m = 9$  and 13 based on wedge-shaped twin boundaries (TBs) fully-occupied with gallium parallel to the  $b$  axis. They assigned the  $Cmc2_1$  space group on the basis of simulation and energy-dispersive x-ray spectroscopy (EDS) techniques. In a single-crystal x-ray diffraction (XRD) study of the  $\text{Ga}_2\text{O}_3(\text{ZnO})_m$  ( $m = 6$  and 9) homologous compounds, Michiue et al.<sup>11</sup> proposed the orthorhombic  $Cmcm$  group for even and odd values of  $m$ .<sup>5,12</sup> Subsequently, it was proposed, by means of HRTEM, that the  $\text{Ga}_2\text{O}_3(\text{ZnO})_9$  homologue<sup>6,12</sup> was formed by stacking of  $m + 1$  Zn-O tetrahedra, IBs and wedge-shaped TBs. The unique

stacking sequence of IB and TB interfaces found in  $\text{Ga}_2\text{O}_3(\text{ZnO})_m$  efficiently scatter phonons, thereby reducing thermal conductivity. The effectiveness of these interfaces to scatter phonons decreased the thermal conductivity to 1.8–1.3 W/m K at 300–900 K when  $m = 9$ , while maintaining an electrical conductivity of 10 S/cm and a Seebeck coefficient of  $-250 \mu\text{V/K}$  at room temperature.<sup>5,12</sup>

The crystal structure of the  $\text{In}_2\text{O}_3(\text{ZnO})_m$  homologous compounds has been widely studied and consists of an alternate stacking of  $\text{InO}_2^-$  octahedral layers with  $(\text{InZn}_m)\text{O}_{m+1}^+$  layers.<sup>13-16</sup> The  $\text{InO}_2^-$  octahedral layer forms an IB, where the polar  $c$  axis of the  $\text{ZnO}_4$  octahedra within the  $(\text{InZn}_m)\text{O}_{m+1}^+$  points backwards towards the  $\text{InO}_2^-$  octahedral layer. A zig-zag, In-rich, modulated IB within the  $(\text{InZn}_m)\text{O}_{m+1}^+$  layer has been proposed theoretically<sup>15,16</sup> and verified experimentally.<sup>13,14</sup> Electronic conduction within the  $\text{In}_2\text{O}_3(\text{ZnO})_m$  homologous compounds has been reported to occur mainly in the  $\text{InO}_2^-$  octahedral layers,<sup>17</sup> leading to a high electrical conductivity of 500 S/cm at 300 K when  $m = 5$ .<sup>9</sup> Due to the highly anisotropic structure of these compounds, texturing is an effective way to enhance their TE response. A very high  $ZT$  of 0.33 was reported in yttria-substituted  $\text{In}_2\text{O}_3(\text{ZnO})_5$  when textured.<sup>9</sup>

In the  $\text{Ga}_2\text{O}_3\text{-ZnO-In}_2\text{O}_3$  ternary system, the homologous compounds with the general formula  $\text{InGa}_2\text{O}_3(\text{ZnO})_m$  ( $m = 2-20$ ) exist.<sup>13,14,18-21</sup> Using single-crystal and powder XRD analysis, a crystal structure closely similar to that of the  $\text{In}_2\text{O}_3(\text{ZnO})_m$  parental compound was proposed by Keller et al.<sup>21</sup> for  $\text{InGaO}_3(\text{ZnO})_3$ , with stacking of  $\text{InO}_2^-$  octahedral layers and  $(\text{GaZn}_m)\text{O}_{m+1}^+$  layers; the  $\text{Ga}^{3+}$  atoms occupy the trigonal bipyramidal positions causing polarity inversion of the  $\text{ZnO}_4$  tetrahedra at positions halfway between the  $\text{InO}_2^-$  octahedral layers. The proposed IB<sup>21</sup> formed by  $\text{Ga}^{3+}$  cations in trigonal bipyramidrons within the  $(\text{GaZn}_m)\text{O}_{m+1}^+$  layer produces a flat boundary lying halfway between the  $\text{InO}_2^-$  octahedral layers.

The crystal structure of the  $\text{In}_{1-x}\text{Ga}_x\text{O}_3(\text{ZnO})_m$  ( $m = 1-5$ ) solid solution has also been reported. It was proposed<sup>18</sup> that the Ga atoms occupy the In sites in  $(\text{InZn}_m)\text{O}_{m+1}^+$  for Ga substitutions equivalent to  $x = 0.0-0.5$ , and start substituting the In positions in the  $\text{InO}_2^-$  octahedral layer when  $x > 0.5$ . Both the high electrical properties of the  $\text{In}_2\text{O}_3(\text{ZnO})_m$  compounds and the very low thermal conductivity of the  $\text{Ga}_2\text{O}_3(\text{ZnO})_m$  compounds encouraged us to investigate the TE properties of the  $(\text{Ga}_{1-x}\text{In}_x)_2\text{O}_3(\text{ZnO})_9$  solid solution. This solid solution should offer the advantage of reducing the processing cost over the  $\text{In}_2\text{O}_3(\text{ZnO})_9$  parent compound without compromising the TE response.

We have investigated the dependence of crystal structure and TE properties on composition in the  $\text{Ga}_2\text{O}_3(\text{ZnO})_9\text{-In}_2\text{O}_3(\text{ZnO})_9$  system. We identified

that co-addition of  $B_2O_3$  and  $Nd_2O_3$  promotes densification in all the compositions. Clear correlations between the changes in the crystal structure and the transport properties have been established.

## EXPERIMENTAL

Ceramics of  $(1-x)Ga_2O_3(ZnO)_9-xIn_2O_3(ZnO)_9$  ( $x = 0.0$  to  $1.0$  in steps of  $0.2$ ) were prepared. The starting powders were reagent-grade ZnO (Prolabo, 99.9%)  $Ga_2O_3$  (PI-KEM Ltd.<sup>®</sup>, 99.995%) and  $In_2O_3$  (PI-KEM Ltd.<sup>®</sup>, 99.99%). The stoichiometric formulations were wet-mixed with propan-2-ol and yttria-stabilised zirconia balls in a 1:1:1 ratio for 24 h, dried for 24 h at 358 K, and then calcined in air at 1523 K for 4 h. After adding 0.2 wt.%  $B_2O_3$  and 0.5 wt.%  $Nd_2O_3$ <sup>8</sup> to the calcined powders, they were wet-mixed again for 24 h and dried. Calcined powders were uniaxially pressed into pellets 20 mm in diameter and 4 mm thick using a hardened steel die. The pellets were covered in sacrificial powder of the same composition and then sintered at 1723 K for 4 h in air; the cooling and heating rates were 180 and 360 K/h, respectively. Densities of the sintered ceramics were determined by the Archimedes method.

Phase identification and structural characterisation of the samples was performed using a PANalytical X'Pert Pro<sup>®</sup> diffractometer in  $\Theta$ - $\Theta$ , Bragg-Brentano geometry with  $CuK_\alpha$  radiation. Samples were scanned in the  $2\theta = 25^\circ$ – $80^\circ$  range with a step size of  $0.017^\circ$ . XRD patterns were refined using TOPAS-Academic V5<sup>®</sup> software.<sup>22</sup>

For microstructure evaluation, specimens were ground and etched then examined using a Philips<sup>®</sup> XL30 field emission gun-scanning electron microscope (FEG-SEM, HKL<sup>®</sup>) microscope equipped with an EDS detector. Samples for TEM observations were crushed in an agate mortar and pestle. Grains of individual powders were dispersed in chloroform, dropped onto a copper grid covered with a holey carbon film, and then dried. Local structural characterisation of the samples was performed with an FEI FEG-transmission electron microscope (Tecnai G2 F30) operating at 300 kV. Atomic-resolution EDS studies were carried out with a FEI Themis electron microscope operated in STEM mode at 200 kV with a Super-X detector system (ChemS-TEM technology) for EDS chemical characterisation. EDS spectrum images were acquired by serially rastering across a defined area of the specimen and recording cumulative EDS spectra at each position. EDS chemical maps were produced by integrating the intensity of the Zn  $K_\alpha$  and Ga  $K_\alpha$  absorption peaks.

The electrical conductivity and Seebeck coefficients were determined as a function of temperature from ambient to 900 K in a helium atmosphere using an ULVAC<sup>®</sup> ZEM-III instrument. Thermal diffusivity was determined from room temperature to 900 K in an argon environment using a Netzsch<sup>®</sup>

LFA 427 laser flash analyser<sup>23</sup>; samples were graphite-coated prior to diffusivity measurements; heat capacity was obtained using a Netzsch<sup>®</sup> STA 449 C in an argon atmosphere. Finally, the thermal conductivity of the samples was calculated from the heat capacity ( $C_p$ ), thermal diffusivity ( $\alpha$ ) and density ( $\rho$ ) via the relationship  $\kappa = \rho\alpha C_p$ .

## RESULTS AND DISCUSSION

With the exception of the  $x = 0.6$  composition, all the  $Ga_{1-x}In_xO_3(ZnO)_9$  ceramics attained a density of at least 90% theoretical. The one low density value of 85% theoretical (for  $x = 0.6$ ) relates to the mid-range of the  $Ga_2O_3(ZnO)_9$  and  $In_2O_3(ZnO)_9$  system. Nevertheless, 85% theoretical density for such compositions is still significantly higher than the values of 50–60% reported by Moriga et al.<sup>18</sup>

Figure 1 shows microstructures of the  $(Ga_{1-x}In_x)_2O_3(ZnO)_9$  polycrystalline ceramics sintered at 1723 K for 4 h. All the samples exhibit plate-like microstructures, typical of these layered compounds.<sup>6–9,24</sup> Additionally, a minor second phase, white in colour, was visible at the grain boundaries in all the samples (examples are circled in red in Fig. 1a). Combined SEM-EDS analyses indicated the minor phases were rich in Nd. The segregation of this phase to the grain boundaries and the improved density (compared to earlier study of the ternary system<sup>18</sup>) suggests that successful liquid-phase sintering was achieved through addition of 0.2 wt.%  $B_2O_3$  and 0.5 wt.%  $Nd_2O_3$ . Stripes parallel to the growth direction are visible in some grains (see Fig. 1c) in agreement with earlier investigations<sup>7</sup>; the number of grains exhibiting these parallel stripes decreases with increasing gallium concentration; the  $x = 1$  sample has a high density of these features (Fig. 1c). The size of grains in ceramics of the  $(Ga_{1-x}In_x)_2O_3(ZnO)_9$  solid solution was independent of composition, being approximately  $57 \mu m$  in all the samples.

Figure 2 shows XRD patterns for the  $(Ga_{1-x}In_x)_2O_3(ZnO)_9$  polycrystalline ceramics. Only peaks for the primary phase could be identified in the patterns. Diffraction data were indexed using a rhombohedral  $R\bar{3}m$  space group proposed by Canard and Tilley<sup>25</sup> and Keller et al.<sup>21</sup> for the  $InGaO_3(ZnO)_9$  compounds and the  $Cmcm$  structure proposed for the  $Ga_2O_3(ZnO)_9$  homologous compounds.<sup>8,11</sup> Even at low indium concentrations ( $x = 0.2$ ), the XRD patterns were indexed successfully using the rhombohedral  $R\bar{3}m$  space group, typical of In-based homologous compounds; no traces of the orthorhombic  $Cmcm$   $Ga_2O_3(ZnO)_9$  variant were detected.

Increasing indium concentrations from  $x = 0.2$  to  $0.4$  caused a decrease in the lattice parameter  $c$  of the samples, whereas high indium concentrations ( $x = 0.6$ – $1.0$ ) lead to an increase of the lattice parameter  $c$ . For low values of  $x$ , these changes are reflected in the movements of the (001)

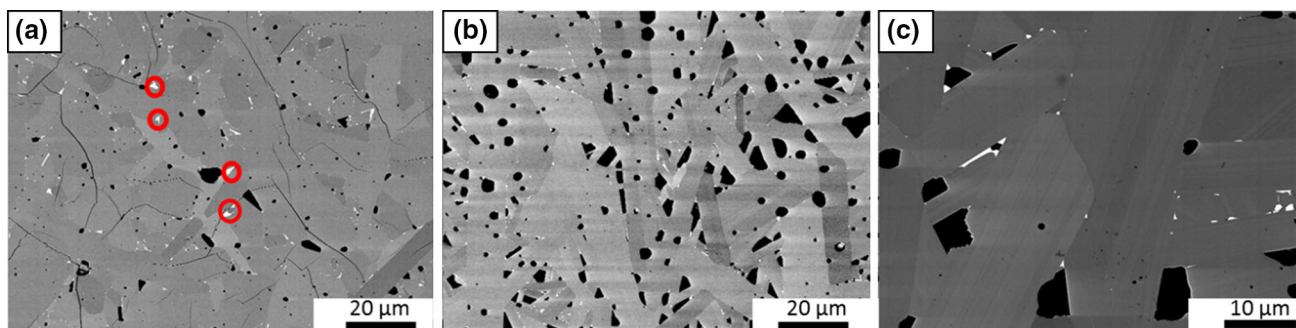


Fig. 1. Back scattered electron (BSE) SEM images of  $(\text{Ga}_{1-x}\text{In}_x)_2\text{O}_3(\text{ZnO})_9$  samples (a)  $x = 0.0$  and (b)  $x = 0.1$ ; (c) high-magnification image of sample  $x = 1.0$ .

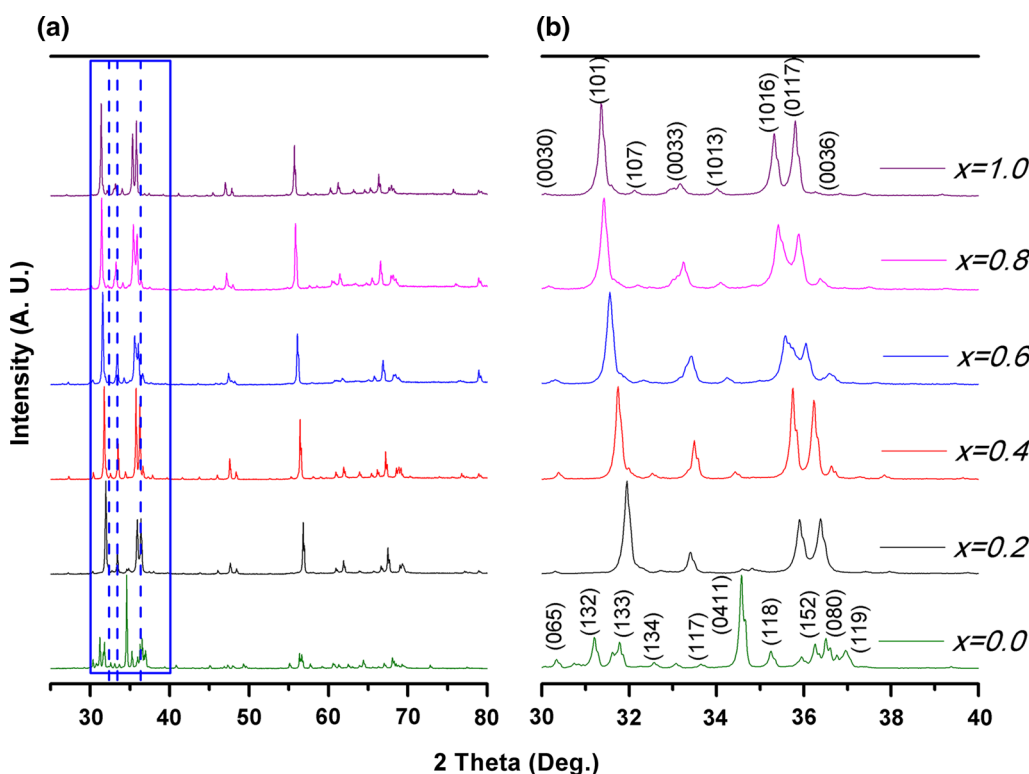


Fig. 2. XRD patterns of the  $(\text{Ga}_{1-x}\text{In}_x)_2\text{O}_3(\text{ZnO})_9$  samples for scan ranges of (a)  $2\theta = 25^\circ\text{--}80^\circ$  and (b)  $2\theta = 30^\circ\text{--}37^\circ$ .

reflections towards higher  $2\theta$  values (Fig. 2b), consistent with the findings of Moriga et al.<sup>18</sup> for the  $\text{Ga}_{1-x}\text{In}_x(\text{ZnO})_m$  ( $m = 3$ ) system. Similarly, at higher indium content, increasing  $x$  from 0.6 to 1.0 displaces the (001) reflections towards lower  $2\theta$  values, indicating an increase in the lattice parameter  $c$ , in agreement with the work of Moriga et al.<sup>18,20</sup> They suggested that at low indium concentrations ( $x < 0.5$ ), the reduction in the lattice parameter  $c$  is due to a compensation effect. When Ga atoms are substituted by In atoms in the  $\text{InO}_2$  layer of the  $\text{In}_2\text{O}_3(\text{ZnO})_m$  homologous compound, an expansion of the  $\text{InO}_2$  layer occurs in the  $a$  direction; this expansion is compensated for by a contraction in the  $c$  direction to maintain the cation–anion distance.<sup>18,20</sup> In contrast, at high indium

**Table I. Lattice parameter  $c$  for  $(\text{Ga}_{1-x}\text{In}_x)_2\text{O}_3(\text{ZnO})_9$  samples from the XRD data ( $c_{\text{XRD}}$ ), and calculated by Nakamura et al.<sup>19</sup> ( $c_{\text{Ref}}$ )**

Sample	$c_{\text{XRD}}$ (Å)	$c_{\text{Ref}}$ (Å) <sup>19</sup>
$\text{Ga}_2\text{O}_3(\text{ZnO})_9$	33.6355 (6)	33.55
$(\text{Ga}_{0.8}\text{In}_{0.2})_2\text{O}_3(\text{ZnO})_9$	88.4495 (4)	88.68
$(\text{Ga}_{0.6}\text{In}_{0.4})_2\text{O}_3(\text{ZnO})_9$	88.2186 (2)	88.61
$(\text{Ga}_{0.4}\text{In}_{0.6})_2\text{O}_3(\text{ZnO})_9$	88.4007 (1)	88.39
$(\text{Ga}_{0.2}\text{In}_{0.8})_2\text{O}_3(\text{ZnO})_9$	88.8735 (5)	88.87
$\text{In}_2\text{O}_3(\text{ZnO})_9$	89.006 (2)	89.25

concentrations ( $x > 0.5$ ), the lattice parameter  $c$  increases with indium concentration since larger indium atoms are substituting for smaller gallium

atoms within the  $(\text{InZn}_m)\text{O}_{m+1}^+$  layer.<sup>18,20</sup> The calculated  $c$  parameters are presented in Table I. The difference between the lattice parameter  $c$  for the  $x = 0.2$  and  $1.0$  samples is small ( $\sim 1$  Å). Nakamura and co-workers<sup>19</sup> predicted the length of the lattice parameter  $c$  ( $c_{\text{Ref}}$  in Table I) to be 88.68 Å and 89.25 Å for  $x = 0.2$  and  $x = 1$ , respectively. They assumed a layered structure stacking  $\text{InO}_2^-$ ,  $(\text{InZn})\text{O}_{2.5}$  and  $(m-1)$  ZnO layers along the  $c$  axis. These calculated values are slightly higher than our experimental values ( $c_{\text{XRD}}$ ), summarised in Table I, but the trend is the same.

To better understand the structural changes induced by indium substitution, HRTEM and selected-area electron diffraction (SAED) analyses were performed. For the  $\text{Ga}_2\text{O}_3(\text{ZnO})_9$  end member, TEM images (e.g. Fig. 3a) revealed wedge-shaped TBs, in agreement with the HRTEM studies of Li et al.<sup>10</sup> For the In-containing samples, the wedge-shaped TBs are no longer observed; instead, equidistant parallel lines perpendicular to the  $c$  axis (Fig. 3b and c) are observed even at low In concentrations ( $x = 0.2$ ). In the images for  $m + 1$ , atomic columns can be found between the parallel lines, in agreement with earlier work on the ZnO- $\text{In}_2\text{O}_3$ -based homologous compounds.<sup>19</sup> The structure for the compound with the lowest indium concentration ( $x = 0.2$ ) shown in Fig. 3b resembles the crystal structure exhibited by the  $\text{In}_2\text{O}_3(\text{ZnO})_m$  compound (Fig. 3c). HRTEM images for the  $\text{In}_2\text{O}_3(\text{ZnO})_9$  end member (e.g. Figure 3c) show equidistant parallel lines perpendicular to the  $c$  axis (IB-I), corresponding to the  $\text{InO}_2^-$  octahedral layer inverting the polarity of the  $\text{ZnO}_4$  tetrahedra along the basal plane.<sup>15,16,21,26</sup> A homogeneous distribution of  $m + 1$  atomic columns is observed between these parallel lines within the  $(\text{InZn}_m)\text{O}_{m+1}^+$  layer, highlighted by yellow spots in Fig. 3c. A less apparent zig-zag shaped structural feature, IB-II in Fig. 3c, can be observed within the  $(\text{InZn}_m)\text{O}_{m+1}^+$  layer. This has been interpreted as an In-rich pyramidal IB with a zig-zag shape, and as

being one dimensional and modulated along the  $b$  axis.<sup>13,14</sup> The presence of the less apparent modulated zig-zagged IB is further confirmed by the appearance of additional satellite reflections around the main reflections in the SAED image shown in Fig. 3c. It is believed that the formation of IBs in the basal plane, triggered by small additions of indium, are energetically more favourable than those in the pyramidal plane induced by gallium additions. The zig-zagged modulated pyramidal IB (IB-II) observed in the  $\text{In}_2\text{O}_3(\text{ZnO})_9$  compound is also preserved in the  $(\text{Ga}_{0.8}\text{In}_{0.2})_2\text{O}_3(\text{ZnO})_9$ . The presence of this type-II IB is further confirmed by the appearance of additional spots in the SAED (Fig. 3b). The TEM results are in good agreement with our XRD patterns.

The crystal structure, the type of IBs, and the distribution of In in the lattice specifically in the IBs is well established.<sup>15,16,21,26</sup> To further distinguish the differences between the structural features exhibited by both end members, we conducted an aberration-corrected microscopy study of the  $\text{Ga}_2\text{O}_3(\text{ZnO})_9$  sample ( $x = 0$ ) to resolve the structure and elemental distribution in the TBs and IBs. Figure 4a shows a high-angle annular dark field (HAADF) STEM image acquired with the incident electron beam parallel to the  $[100]$  direction; the image reveals a head-to-head type twinned nanostructure, with a wedge apex angle of  $\sim 63.37^\circ$  (marked in Fig. 4a). The boundaries of the twins, labelled as TB in Fig. 3a, are parallel to the  $b$  axis of the crystal structure. The width of the twins deduced from the lattice images is  $\sim 33$  Å, in agreement with HRTEM (see Fig. 3a). The well-ordered nano-TBs are marked with parallel white lines (Fig. 4b). The  $m + 1 = 10$  atomic columns between the wedge-shaped nano-TBs are observed, as reported by Li et al.<sup>10</sup> in the earlier HRTEM study. The width of the nano-twins is uniform throughout the region screened in Fig. 3, corresponding to  $m + 1 = 10$  atomic columns. The stacking sequence in the modular structure of the  $\text{Ga}_2\text{O}_3(\text{ZnO})_m$  compounds must be described by

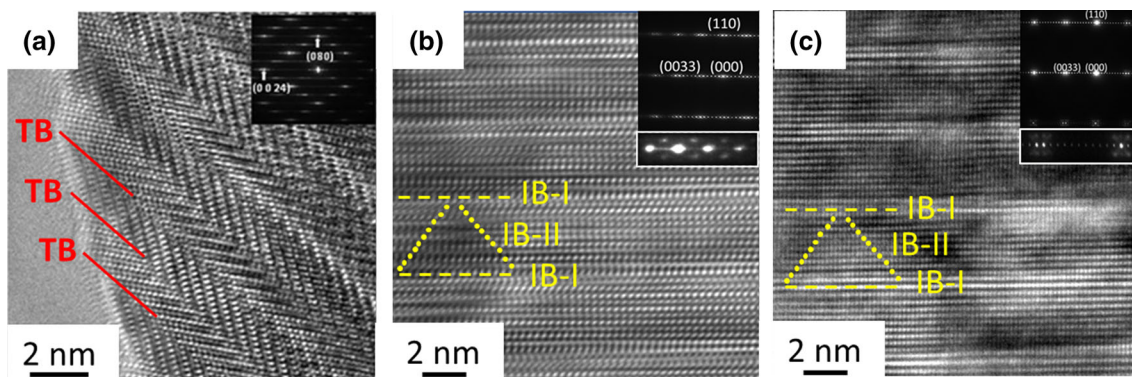


Fig. 3. (a) HRTEM  $[100]$  image of  $\text{Ga}_2\text{O}_3(\text{ZnO})_9$ , (b) HRTEM  $[110]$  image of  $(\text{Ga}_{0.8}\text{In}_{0.2})_2\text{O}_3(\text{ZnO})_9$  and (c) HRTEM image of  $\text{In}_2\text{O}_3(\text{ZnO})_9$  homologous compound. The insets in the images show the corresponding SAED. Satellite reflections can be observed in (b) at the bottom of the enlarged SAED.

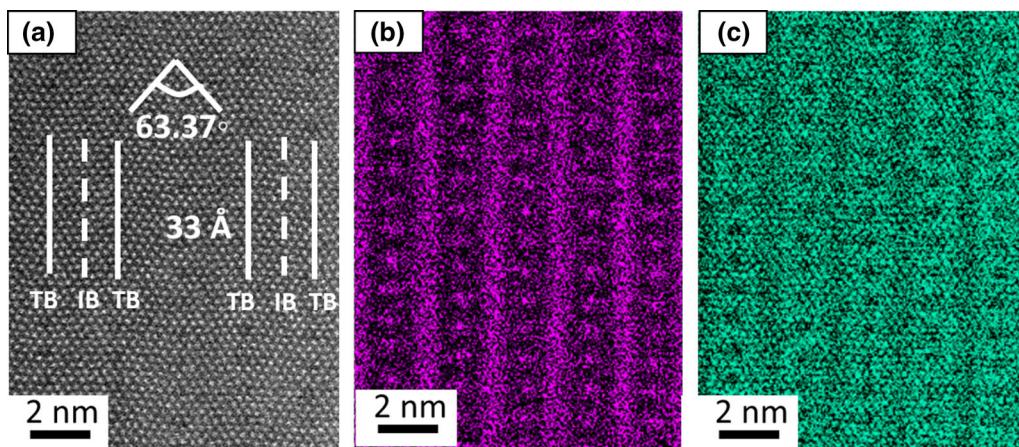


Fig. 4. (a) [100] HAADF image of the  $\text{Ga}_2\text{O}_3(\text{ZnO})_9$  ( $x = 0$ ) sample and corresponding EDS elemental maps: (b) Ga- $K_x$  and (c) Zn- $K_x$ .

considering both the TBs and IBs as structural building operators.<sup>6,8,11,12</sup>

The distribution of Zn and Ga in the  $\text{Ga}_2\text{O}_3(\text{ZnO})_9$  structure was investigated by atomically resolved STEM-EDS (for clarity, only the Ga map is shown in Fig. 4b); the maps reveal the prevalence of Ga (and corresponding Zn depletion) at the TB, more specifically by the darker atomic columns in the HAADF image (Fig. 4a). The Ga partially occupied TB observed in the HAADF-EDS maps (Fig. 4b and c) shows that Ga and Zn occupy the alternate lattice sites in the TBs. This finding is in good agreement with the predictions of Barf et al.<sup>27</sup> and Guilmeau et al.<sup>6</sup> in the HAADF-STEM-EDS studies of low-level Ga-doped ZnO. Furthermore, Ga-enriched bands can be observed parallel and between the TBs (Fig. 4b). These Ga-rich boundaries can be inferred as IBs. Thus, the EDS data suggests the formation of Ga-containing IBs between the nano-TBs.

The TE properties of the  $(1-x)\text{Ga}_2\text{O}_3(\text{ZnO})_9$ - $x\text{In}_2\text{O}_3(\text{ZnO})_9$  solid solution system were determined, and are summarised in Fig. 5. All the Ga-containing samples show semiconducting behaviour, with electrical conductivity of 5–20 S/cm at room temperature. However, the  $\text{In}_2\text{O}_3(\text{ZnO})_9$  end member shows metallic behaviour with the highest electrical conductivity of around 85 S/cm at room temperature; this is comparable with data reported by Ohta et al.<sup>7</sup> for this end member. Overall, the electrical conductivity increases across the whole temperature range upon the introduction of In into the structure. Remarkably, the rate of increase of electrical conductivity with increasing temperature is more pronounced for the composition with  $x = 0.2$ , reaching a high value of 50 S/cm at 900 K. It is believed that the reason for this beneficial increase in the electrical conductivity of the  $(\text{Ga}_{0.8}\text{In}_{0.2})_2\text{O}_3(\text{ZnO})_9$  sample, is due to (a) the change in the crystal structure from wedge-shaped TBs to planar IBs and (b) a reduction in the electronic band gap.<sup>28</sup> The change in the crystal structure was

triggered by the formation of both type I and type II IBs, creating a crystal structure similar to that of the  $\text{In}_2\text{O}_3(\text{ZnO})_9$  end member, as observed in Fig. 3b. At high gallium concentration ( $x < 0.5$ ), the IB-I, where the electrical conduction mainly occurs,<sup>17,20</sup> will be highly doped by gallium. This substitution was previously proposed by Nakamura et al.<sup>19</sup> and further confirmed by the systematic change in the lattice parameter  $c$  in our XRD data (Fig. 2). In addition to the modification of the crystal structure (Fig. 3), the substitution of Ga at In sites may induce a change in the electronic band structure of the  $\text{Ga}_{1-x}\text{In}_x\text{O}_3(\text{ZnO})_9$  compound due to the formation of localised band edge states by Ga additions.<sup>28</sup> The higher electrical conductivity at  $x = 0.2$  (Fig. 5a) further suggests the narrowing of the electronic band gap by the isoelectronic substitution of In by Ga at the IBs. Further increase in the indium concentration ( $x = 0.4$ ) also produces a high rate of increase of the electrical conductivity with increasing temperature, but less pronounced compared to samples with  $x = 0.2$  (Fig. 5). Additionally, the room-temperature electrical conductivity of In-substituted compositions depends on the In–O bond length found in the  $\text{InO}_2$  layer (IB-I); the larger the In–O distance, the higher the electrical conductivity, as shown in Fig. 5a; this was proposed by Moriga et al.<sup>20</sup> for the  $\text{InGaO}_3(\text{ZnO})_m$   $m = 1, 3$  and  $5$  systems.

The Seebeck coefficients of the  $(\text{Ga}_{1-x}\text{In}_x)_2\text{O}_3(\text{ZnO})_9$  solid solution samples (Fig. 5b) exhibit  $n$ -type behaviour and the absolute values ( $|S|$ ) increase with increasing temperature. Among all the compositions, the  $\text{In}_2\text{O}_3(\text{ZnO})_9$  end member shows the lowest  $|S|$  which increased from 80  $\mu\text{V/K}$  to 150  $\mu\text{V/K}$  over the temperature range, inversely proportional to the higher electrical conductivity exhibited by this sample. The Seebeck coefficients for the  $\text{In}_2\text{O}_3(\text{ZnO})_9$  sample are in good agreement with the values reported by Ohta et al.<sup>7</sup> Within the uncertainty range, the Ga-based samples ( $x = 0.4, 0.6$  and  $0.8$ ) have approximately the same Seebeck

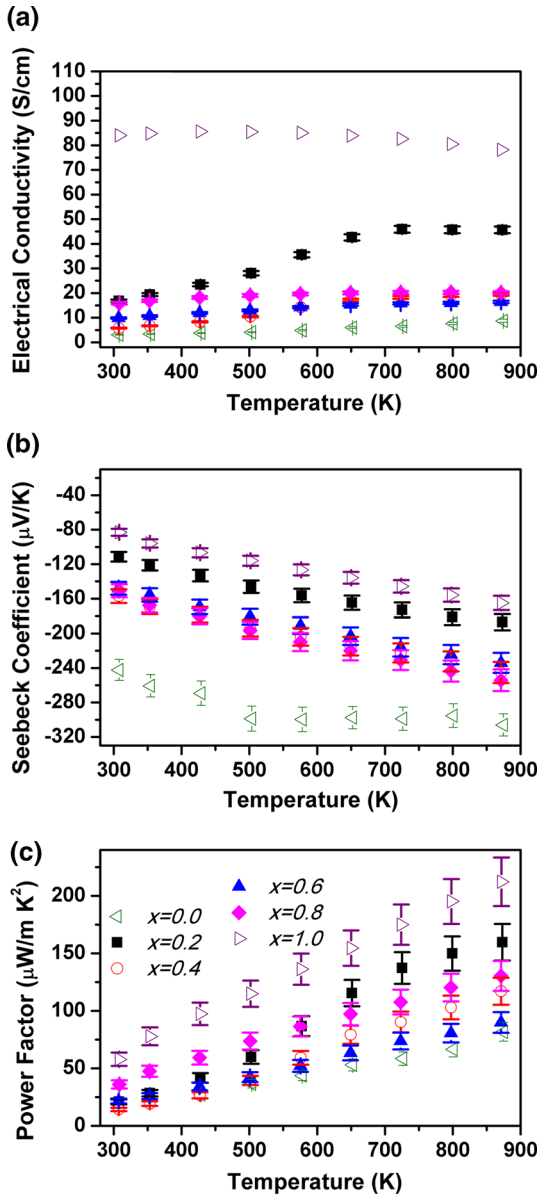


Fig. 5. (a) Electrical conductivity, (b) Seebeck coefficient and (c) power factor of  $\text{Ga}_{1-x}\text{In}_x)_2\text{O}_3(\text{ZnO})_9$  samples: green left-pointing small triangle  $x = 0.0$ , filled square  $x = 0.2$ , red circle  $x = 0.4$ , blue triangle  $x = 0.6$ , pink diamond  $x = 0.8$  and purple right-pointing small triangle  $x = 1.0$  (Color figure online).

coefficients ( $|S|$ ) which increase from  $\sim 150 \mu\text{V/K}$  at room temperature to  $\sim 250 \mu\text{V/K}$  at 900 K. The  $x = 0.2$  sample,  $(\text{Ga}_{0.8}\text{In}_{0.2})_2\text{O}_3(\text{ZnO})_9$ , shows a slightly lower absolute value of the Seebeck coefficient, increasing from 110 to 180  $\mu\text{V/K}$  over the temperature range tested. These results are consistent with the higher electrical conductivity exhibited by this sample ( $x = 0.2$ ).

The power factors for the  $(\text{Ga}_{1-x}\text{In}_x)_2\text{O}_3(\text{ZnO})_9$  solid solution samples are presented in Fig. 5c. Among the Ga-based compounds, the  $(\text{Ga}_{0.8}\text{In}_{0.2})_2\text{O}_3(\text{ZnO})_9$  sample exhibited a much higher power factor of approximately 150  $\mu\text{W/m K}^2$  at

900 K compared to that of the  $\text{Ga}_2\text{O}_3(\text{ZnO})_9$  end member (75  $\mu\text{W/m K}^2$  at 900 K).

The thermal conductivity data for the  $(\text{Ga}_{1-x}\text{In}_x)_2\text{O}_3(\text{ZnO})_9$  samples are shown in Fig. 6a; all are less than 4 W/m K at 300 K, which is much lower than for pure ZnO and most oxide-based TE materials. The thermal conductivity of the  $\text{Ga}_{1-x}\text{In}_x)_2\text{O}_3(\text{ZnO})_9$  samples gradually increased as the In concentration increased, reaching 3.7 W/m K for  $x = 1$  at room temperature. The thermal conductivity of the  $x = 0.6$  sample is slightly lower than that of the  $x = 0.2$  sample; this might be due to lower density of the  $x = 0.6$  sample ( $\sim 85\%$ ). Moreover, considering Maxwell density corrections and the electronic contribution to the thermal conductivity, the lattice contribution to the thermal conductivity also increases as the In concentration increases in the  $(\text{Ga}_{1-x}\text{In}_x)_2\text{O}_3(\text{ZnO})_9$  system. This is attributed to the introduction of point defects at the interfaces (IB-I and IB-II). The thermal conductivity of the In-based compound is twice that of the Ga-based compound. However, low indium concentrations in the  $(\text{Ga}_{1-x}\text{In}_x)_2\text{O}_3(\text{ZnO})_9$  system significantly lowers the thermal conductivity of the  $\text{In}_2\text{O}_3(\text{ZnO})_9$  compound, approaching that of  $\text{Ga}_2\text{O}_3(\text{ZnO})_9$ . This decrease in the thermal conductivity is ascribed to increased phonon scattering centres introduced through doping and the decreased distance between the parallel interfaces IB-I ( $\text{InO}_2^-$  layer) when gallium substitutes for indium.

The thermal conductivity of  $\text{In}_2\text{O}_3(\text{ZnO})_9$  ( $x = 1.0$ ), Fig. 6a, is 12% lower than the value reported by Ohta et al.<sup>7</sup> The calcination step and longer sintering time used in this study may be the reason for this beneficial reduction. However, the mechanism lowering the thermal conductivity of our high-density sample cannot be identified by simple comparison with the work of Ohta et al.,<sup>7</sup> due to the lack of structural data and microstructure details in their study.

The ZT for all the samples was determined from the power factor and thermal conductivity data (Figs. 5 and 6a) and is plotted in Fig. 6b. In the In-substituted samples, a high ZT of 0.07 at 900 K was obtained for  $(\text{Ga}_{0.8}\text{In}_{0.2})_2\text{O}_3(\text{ZnO})_9$  sample. This is due to an improved power factor while maintaining the low thermal conductivity of  $(\text{Ga}_2\text{O}_3(\text{ZnO})_9$  achieved by engineering the interfaces at the nanoscale level and potentially by nanoparticles arising from the Nd and B additions. The reduced thermal conductivity of composition  $x = 0.2$  is ascribed to increased phonon scattering centres introduced through mass difference and the reduction in the spacing of the interfaces. The high ZT for the  $x = 0.2$  sample (Fig. 6b) of 0.07 is the highest reported for the In and Ga homologous compounds;  $(\text{Ga}_{1-x}\text{In}_x)_2\text{O}_3(\text{ZnO})_m$  ( $x = 0.5$ ,  $m = 1, 3$  and  $5$ )<sup>8,20</sup> and  $\text{In}_2\text{O}_3(\text{ZnO})_9$ . This high ZT of 0.07 at 900 K arises from the lower thermal conductivity

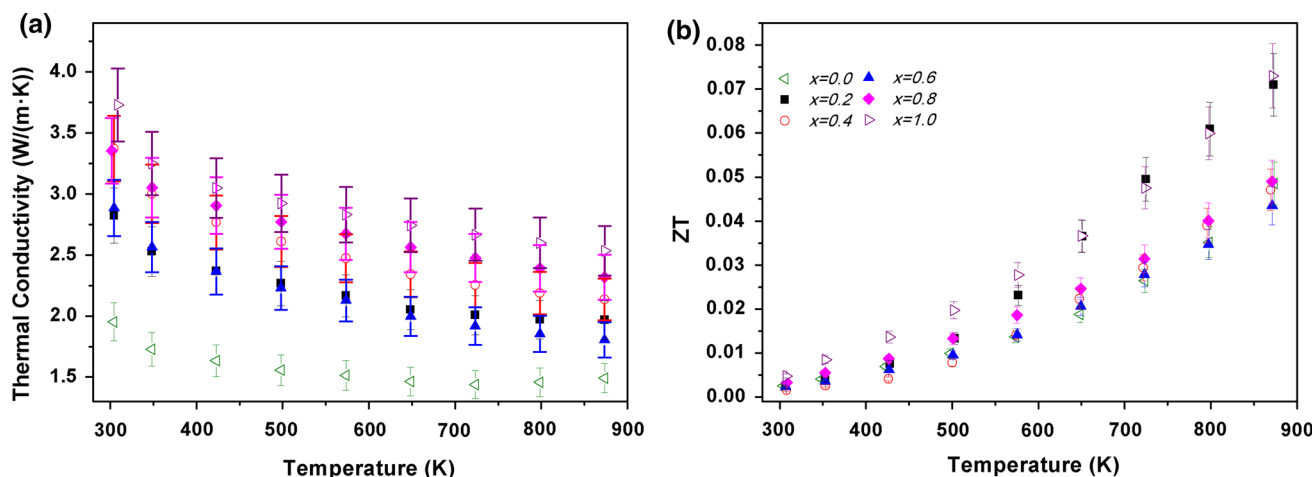


Fig. 6. (a) Thermal conductivity and (b) dimensionless figure of merit of  $(\text{GaIn}_{1-x}\text{In}_x)_2\text{O}_3(\text{ZnO})_9$  samples: green left-pointing small triangle  $x = 0.0$ , filled square  $x = 0.2$ , red circle  $x = 0.4$ , blue triangle  $x = 0.6$ , pink diamond  $x = 0.8$  and purple right-pointing small triangle  $x = 1.0$  (Color figure online).

exhibited by the high-density  $\text{In}_2\text{O}_3(\text{ZnO})_9$  compound prepared with 0.2 wt.%  $\text{B}_2\text{O}_3$  and 0.5 wt.%  $\text{Nd}_2\text{O}_3$ .

## CONCLUSIONS

High-density ceramics in the  $(\text{Ga}_{1-x}\text{In}_x)_2\text{O}_3(\text{ZnO})_9$  system were achieved by the use of minor additions of  $\text{B}_2\text{O}_3$  and  $\text{Nd}_2\text{O}_3$  to promote densification. The structural features of Ga-based compounds are different from the In-based compounds. The  $\text{Ga}_2\text{O}_3(\text{ZnO})_9$  stacks TBs and IBs along the  $c$  axis, whereas the  $\text{In}_2\text{O}_3(\text{ZnO})_9$  is formed by the stacking of basal and pyramidal IBs.<sup>26</sup> It was found that even at low indium concentrations ( $x = 0.2$ ), the crystal structure of the  $(\text{Ga}_{1-x}\text{In}_x)_2\text{O}_3(\text{ZnO})_9$  homologue resembles that of the  $\text{In}_2\text{O}_3(\text{ZnO})_m$  end member rather than its gallium counterpart. The sample with the lowest indium concentration ( $x = 0.2$ ) exhibited basal and pyramidal zig-zag shaped IBs, typically found in the  $\text{In}_2\text{O}_3(\text{ZnO})_m$  family. The presence of gallium and indium at these IBs increased the number of scattering centres, lowering the thermal conductivity. Substitution of small amounts of In [i.e.  $(\text{Ga}_{0.8}\text{In}_{0.2})_2\text{O}_3(\text{ZnO})_9$   $x = 0.2$ ] significantly improved the TE properties of the  $\text{Ga}_2\text{O}_3(\text{ZnO})_9$  end member; Seebeck coefficients increased from 160 to 185  $\mu\text{V}/\text{K}$  at 900 K, electrical conductivity increased from  $\sim 5$  to 40 S/cm at 900 K while maintaining a low thermal conductivity of 2 W/m K at 900 K leading to a high ZT of 0.07 at 900 K; this is the highest ZT reported for both Ga- and In-based homologous compounds. The ZT of the  $x = 0.2$  sample is as high as that for samples of  $\text{In}_2\text{O}_3(\text{ZnO})_9$ , with the added benefit of reduced processing costs through engineering the interfaces at the nanoscale level.

## ACKNOWLEDGMENTS

The authors are grateful to the EPSRC for the provision of funding for this work (EP/H043462, EP/

I036230/1, EP/L014068/1, EP/L017695/1 are acknowledged by RF). SuperSTEM is the EPSRC National Facility for Advanced Electron Microscopy, supported by EPSRC. All research data supporting this publication are directly available within the publication.

## REFERENCES

- H.J. Goldsmid and R.W. Douglas, *Br. J. Appl. Phys.* 11, 386 (1954).
- V.E. Altenkirch, *Phys. Zeitschr.* 16, 10 (1909).
- V.E. Altenkirch, *Physik. Zeitschr.* 12, 920 (1911).
- S.R. Yeandel, M. Molinari, and S.C. Parker, *RSC Adv.* 6, 115 (2016).
- Y. Michiue, T. Mori, A. Prytuliak, Y. Matsushita, M. Tanaka, and N. Kimizuka, *RSC Adv.* 1, 1788 (2011).
- E. Guilmeau, P. Díaz-Chao, O.I. Lebedev, A. Rečnik, M.C. Schäfer, F. Delorme, F. Giovannelli, M. Košir, and S. Bernik, *Inorg. Chem.* 56, 1 (2017).
- H. Ohta, W.S. Seo, and K. Koumoto, *J. Am. Ceram. Soc.* 79, 8 (1996).
- D.T. Alvarez-Ruiz, F. Azough, D. Hernandez-Maldonado, D.M. Kepaptsoglou, Q.M. Ramasse, S.J. Day, P. Svec, P. Svec Sr, and R. Freer, *J. Alloys Compd.* 762, 892 (2018).
- S. Isobe, T. Tani, Y. Masuda, W.S. Seo, and K. Koumoto, *Jpn. J. Appl. Phys.* 2R, 41 (2002).
- C. Li, Y. Bando, M. Nakamura, M. Onoda, and N. Kimizuka, *J. Solid State Chem.* 139, 2 (1998).
- Y. Michiue and N. Kimizuka, *Acta Crystallogr Sec B* 66, 2 (2010).
- D.T. Alvarez-Ruiz, Doctoral Thesis, University of Manchester (2018).
- C. Li, Y. Bando, M. Nakamura, and N. Kimizuka, *J Electron Microsc.* 46, 2 (1997).
- C. Li, Y. Bando, M. Nakamura, M. Onoda, and N. Kimizuka, *J. Solid State Chem.* 139, 2 (1998).
- Y. Yan, L.F. Juarez-Da Silva, S.H. Wei, and M. Al-Jassim, *Appl. Phys. Lett.* 90, 26 (2007).
- Y. Yan, A. Walsh, L.F. Juarez-Da Silva, S.H. Wei, and M. Al-Jassim, in *34th IEEE Photovoltaic Specialists Conference (2009)*, pp. 000172–000174.
- A. Yoshinari, K. Ishida, K.I. Murai, and T. Moriga, *Mater. Res. Bull.* 44, 2 (2009).
- T. Moriga, D.R. Kammler, T.O. Mason, G.B. Palmer, and K.R. Poepplmeier, *J. Am. Ceram. Soc.* 82, 10 (1999).
- M. Nakamura, N. Kimizuka, and T. Mori, *J. Solid State Chem.* 93, 2 (1991).



20. T. Moriga, K. Ishida, K. Yamamoto, A. Yoshinari, and K.I. Murai, *Mater. Res. Innov.* 13, 3 (2009).
21. I. Keller, W. Assenmacher, G. Schnakenburg, W. Mader, and Z. Anorg, *Allg. Chem.* 635, 12 (2009).
22. A. Coelho, *Topas Academic V5* (Australia: Brisbane, 2014).
23. R. Taylor, *J Phys E.* 13, 11 (1980).
24. S.W. Yoon, J.H. Seo, T.Y. Seong, T.H. Yu, Y.H. You, K.B. Lee, H. Kwon, and J.P. Ahn, *J Cryst Growth* 12, 3 (2012).
25. P.J. Cannard and R.J.D. Tilley, *J. Solid State Chem.* 73, 2 (1988).
26. J.B. Labegorre, O.I. Lebedev, C. Bourge, A. Recnik, M. Kossir, S. Bernik, A. Maignan, T. Le Mercier, L. Pautrot-d'Alencon, and E. Guilmeau, *ACS Appl. Mater. Interfaces* 10, 6415 (2018).
27. J. Barf, T. Walther, and W. Mader, *Int Sci.* 12, 2 (2004).
28. Y. Liu, W. Xu, D.-B. Liu, M. Yu, Y.-H. Lin, and C.-W. Nan, *PCCP* 17, 11229 (2015).